

Discovery of a Radiation Component from the Vela Pulsar Reaching 20 Teraelectronvolts

The H.E.S.S. Collaboration: F. Aharonian^{1,2}, F. Ait Benkhali³, J. Aschersleben⁴, H. Ashkar⁵, M. Backes^{6,7}, V. Barbosa Martins⁸, R. Batzofin⁹, Y. Becherini^{10,11}, D. Berge^{8,12}, K. Bernlöhr², B. Bi¹³, M. Böttcher⁷, C. Boisson¹⁴, J. Bolmont¹⁵, M. de Bony de Lavergne¹⁶, J. Borowska¹², F. Bradascio¹⁷, M. Breuhaus², R. Brose¹, F. Brun¹⁷, B. Bruno¹⁸, T. Bulik¹⁹, C. Burger-Scheidlin¹, T. Bylund¹¹, F. Cangemi¹⁵, S. Caroff¹⁵, S. Casanova²⁰, J. Celic¹⁸, M. Cerruti¹⁰, T. Chand⁷, S. Chandra⁷, A. Chen⁹, O. Chibueze⁷, G. Cotter²¹, J. Damascene Mbarubucyeye⁸, A. Djannati-Atai¹⁰, A. Dmytriiev¹⁴, K. Egberts²², J.-P. Ernenwein²³, K. Feijen²⁴, A. Fiasson¹⁶, G. Fichet de Clairfontaine¹⁴, G. Fontaine⁵, M. Füßling⁸, S. Funk¹⁸, S. Gabici¹⁰, Y.A. Gallant²⁵, S. Ghafourizadeh³, G. Giavitto⁸, L. Giunti^{10,17}, D. Glawion¹⁸, J.F. Glicenstein¹⁷, P. Goswami⁷, G. Grolleron¹⁵, M.-H. Grondin²⁶, L. Haerer², M. Haupt⁸, J.A. Hinton², W. Hofmann², T. L. Holch⁸, M. Holler²⁷, D. Horns²⁸, Zhiqiu Huang², M. Jamrozny²⁹, F. Jankowsky³, V. Joshi¹⁸, I. Jung-Richardt¹⁸, E. Kasai⁶, K. Katarzyński³⁰, B. Khélifi¹⁰, S. Klepser⁸, W. Kluźniak³¹, Nu. Komin⁹, K. Kosack¹⁷, D. Kostunin⁸, R.G. Lang¹⁸, S. Le Stum²³, A. Lemièrè¹⁰, M. Lemoine-Goumard²⁶, J.-P. Lenain¹⁵, F. Leuschner¹³, T. Lohse¹², A. Luashvili¹⁴, I. Lypova³, J. Mackey¹, D. Malyshev¹³, D. Malyshev¹⁸, V. Marandon², P. Marchegiani⁹, A. Marcowith²⁵, P. Marinos²⁴, G. Martí-Devesa²⁷, R. Marx³, G. Maurin¹⁶, M. Meyer²⁸, A. Mitchell^{18,2}, R. Moderski³¹, L. Mohrmann², A. Montanari¹⁷, E. Moulin¹⁷, J. Müller⁵, T. Murach⁸, K. Nakashima¹⁸, M. de Naurois⁵, J. Niemiec²⁰, A. Priyana Noel²⁹, P. O'Brien³², S. Ohm⁸, L. Olivera-Nieto², E. de Ona Wilhelmi⁸, M. Ostrowski²⁹, S. Panny²⁷, M. Panter², R.D. Parsons¹², G. Peron², S. Pita¹⁰, D.A. Prokhorov⁴, H. Prokoph⁸, G. Pühlhofer¹³, M. Punch^{10,11}, A. Quirrenbach³, P. Reichherzer¹⁷, A. Reimer²⁷, O. Reimer²⁷, M. Renaud²⁵, F. Rieger², G. Rowell²⁴, B. Rudak³¹, E. Ruiz-Velasco², V. Sahakian³³, S. Sailer², H. Salzmänn¹³, D.A. Sanchez¹⁶, A. Santangelo¹³, M. Sasaki¹⁸, F. Schüssler¹⁷, U. Schwanke¹², J.N.S. Shapopi⁶, A. Sinha²⁵, H. Sol¹⁴, A. Specovius¹⁸, S. Spencer¹⁸, M. Spir-Jacob¹⁰, L. Stawarz²⁹, R. Steenkamp⁶, S. Steinmassl², C. Steppa²², I. Sushch⁷, H. Suzuki³⁴, T. Takahashi³⁵, T. Tanaka³⁴, T. Tavernier¹⁷, R. Terrier¹⁰, C. Thorpe-Morgan¹³, M. Tluczykont²⁸, M. Tsirou², N. Tsuji³⁶, C. van Eldik¹⁸, M. Vecchi⁴, J. Veh¹⁸, C. Venter⁷, J. Vink⁴, S.J. Wagner³, F. Werner², R. White², A. Wierzcholska²⁰, Yu Wun Wong¹⁸, H. Yassin⁷, M. Zacharias^{14,7}, D. Zargaryan¹, A.A. Zdziarski³¹, A. Zech¹⁴, S.J. Zhu⁸, S. Zouari¹⁰, N. Żywucka⁷
and
R. Zanin³⁷, M. Kerr³⁸, S. Johnston³⁹, R.M. Shannon^{39,40,41}, D.A. Smith^{42,43}

1. *Dublin Institute for Advanced Studies, 31 Fitzwilliam Place, Dublin 2, Ireland*
2. *Max-Planck-Institut für Kernphysik, P.O. Box 103980, D 69029 Heidelberg, Germany*
3. *Landessternwarte, Universität Heidelberg, Königstuhl, D 69117 Heidelberg, Germany*
4. *GRAPPA, Anton Pannekoek Institute for Astronomy, University of Amsterdam, Science*

- Park 904, 1098 XH Amsterdam, The Netherlands
5. Laboratoire Leprince-Ringuet, École Polytechnique, CNRS, Institut Polytechnique de Paris, F-91128 Palaiseau, France
 6. University of Namibia, Department of Physics, Private Bag 13301, Windhoek 10005, Namibia
 7. Centre for Space Research, North-West University, Potchefstroom 2520, South Africa
 8. DESY, D-15738 Zeuthen, Germany
 9. School of Physics, University of the Witwatersrand, 1 Jan Smuts Avenue, Braamfontein, Johannesburg, 2050 South Africa
 10. Université de Paris, CNRS, Astroparticule et Cosmologie, F-75013 Paris, France
 11. Department of Physics and Electrical Engineering, Linnaeus University, 351 95 Växjö, Sweden
 12. Institut für Physik, Humboldt-Universität zu Berlin, Newtonstr. 15, D 12489 Berlin, Germany
 13. Institut für Astronomie und Astrophysik, Universität Tübingen, Sand 1, D 72076 Tübingen, Germany
 14. Laboratoire Univers et Théories, Observatoire de Paris, Université PSL, CNRS, Université de Paris, 92190 Meudon, France
 15. Sorbonne Université, Université Paris Diderot, Sorbonne Paris Cité, CNRS/IN2P3, Laboratoire de Physique Nucléaire et de Hautes Energies, LPNHE, 4 Place Jussieu, F-75252 Paris, France
 16. Université Savoie Mont Blanc, CNRS, Laboratoire d'Annecy de Physique des Particules - IN2P3, 74000 Annecy, France
 17. IRFU, CEA, Université Paris-Saclay, F-91191 Gif-sur-Yvette, France
 18. Friedrich-Alexander-Universität Erlangen-Nürnberg, Erlangen Centre for Astroparticle Physics, Erwin-Rommel-Str. 1, D 91058 Erlangen, Germany
 19. Astronomical Observatory, The University of Warsaw, Al. Ujazdowskie 4, 00-478 Warsaw, Poland
 20. Instytut Fizyki Jądrowej PAN, ul. Radzikowskiego 152, 31-342 Kraków, Poland
 21. University of Oxford, Department of Physics, Denys Wilkinson Building, Keble Road, Oxford OX1 3RH, UK
 22. Institut für Physik und Astronomie, Universität Potsdam, Karl-Liebknecht-Strasse 24/25, D 14476 Potsdam, Germany
 23. Aix Marseille Université, CNRS/IN2P3, CPPM, Marseille, France
 24. School of Physical Sciences, University of Adelaide, Adelaide 5005, Australia
 25. Laboratoire Univers et Particules de Montpellier, Université Montpellier, CNRS/IN2P3, CC 72, Place Eugène Bataillon, F-34095 Montpellier Cedex 5, France
 26. Université Bordeaux, CNRS, LP2I Bordeaux, UMR 5797, F-33170 Gradignan, France
 27. Institut für Astro- und Teilchenphysik, Leopold-Franzens-Universität Innsbruck, A-6020 Innsbruck, Austria
 28. Universität Hamburg, Institut für Experimentalphysik, Luruper Chaussee 149, D 22761 Hamburg, Germany
 29. Obserwatorium Astronomiczne, Uniwersytet Jagielloński, ul. Orła 171, 30-244 Kraków, Poland
 30. Institute of Astronomy, Faculty of Physics, Astronomy and Informatics, Nicolaus Copernicus University, Grudziadzka 5, 87-100 Toruń, Poland
 31. Nicolaus Copernicus Astronomical Center, Polish Academy of Sciences, ul. Bartycka 18,

00-716 Warsaw, Poland

32. Department of Physics and Astronomy, The University of Leicester, University Road, Leicester, LE1 7RH, United Kingdom

33. Yerevan Physics Institute, 2 Alikhanian Brothers St., 375036 Yerevan, Armenia

34. Department of Physics, Konan University, 8-9-1 Okamoto, Higashinada, Kobe, Hyogo 658-8501, Japan

35. Kauli Institute for the Physics and Mathematics of the Universe (WPI), The University of Tokyo Institutes for Advanced Study (UTIAS), The University of Tokyo, 5-1-5 Kashiwanoha, Kashiwa, Chiba, 277-8583, Japan

36. RIKEN, 2-1 Hirosawa, Wako, Saitama 351-0198, Japan

37. Cherenkov Telescope Array Observatory gGmbH, Via Gobetti, Bologna, Italy

38. Space Science Division, Naval Research Laboratory, Washington 20375-5352, USA

39. CSIRO Astronomy and Space Science, Australia Telescope National Facility, PO Box 76, Epping, NSW 1710, Australia

40. Centre for Astrophysics and Supercomputing, Swinburne University of Technology Mail H30, PO Box 218, Hawthorn, VIC 3122, Australia

41. ARC Centre of Excellence for Gravitational Wave Discovery (OzGrav), Australia

42. Centre d'Etudes Nucléaires de Bordeaux Gradignan, IN2P3/CNRS, Université de Bordeaux 1, BP120, F-33175 Gradignan Cedex, France

43. Laboratoire d'Astrophysique de Bordeaux, Université de Bordeaux, CNRS, B18N, allée Geoffroy Saint-Hilaire, F-33615 Pessac, France

Corresponding authors: djannati@in2p3.fr, emma.de.ona.wilhelmi@desy.de, bronek@ncac.torun.pl, christo.venter@nwu.ac.za, contact.hess@hess-experiment.eu

Gamma-ray observations have established energetic isolated pulsars as outstanding particle accelerators and antimatter factories in the Galaxy. There is, however, no consensus regarding the acceleration mechanisms and the radiative processes at play, nor the locations where these take place. The spectra of all observed gamma-ray pulsars to date show strong cutoffs or a break above energies of a few gigaelectronvolt (GeV). Using the H.E.S.S. array of Cherenkov telescopes, we discovered a novel radiation component emerging beyond this generic GeV cutoff in the Vela pulsar's broadband spectrum. The extension of gamma-ray pulsation energies up to at least 20 teraelectronvolts (TeV) shows that Vela pulsar can accelerate particles to Lorentz factors higher than 4×10^7 . This is an order of magnitude larger than in the case of the Crab pulsar, the only other pulsar detected in the TeV energy range. Our results challenge the state-of-the-art models for high-energy emission of pulsars while providing a new probe, i.e. the energetic multi-TeV component, for constraining the acceleration and emission processes in their extreme energy limit.

Pulsars, the progeny of supernova explosions, are rapidly spinning and strongly magnetized neutron stars that emit beams of electromagnetic radiation modulated at the

stellar rotational period. Their radiation spans a wide range of frequencies – from the radio domain, where more than 3,000 pulsars are known [1], to high-energy (HE; 100 MeV–100 GeV) gamma rays, where the number of identified or discovered pulsars exceeds 270 [2]. Gamma rays are widely believed to be emitted by electrons and positrons (electrons, hereafter) accelerated to TeV energies at the expense of the neutron star’s rotational energy. However, there is no consensus yet as to the origin of the observed pulsed signals.

Gamma rays in the HE range have proven to be essential probes of pulsar magnetospheres. Indeed, measurements of the spectra of bright gamma-ray pulsars by space-borne telescopes (*EGRET* [3, 4] and *Fermi*-LAT [2]) have established strong (i.e. exponential) cutoffs at energies beyond a few GeV. The cutoffs are not as abrupt as expected in magnetic photon absorption or photon splitting scenarios near the stellar poles, thus ruling out those regions as possible production sites for GeV photons [5, 6]. Very-high-energy (VHE; >100 GeV) gamma rays are invaluable tools for testing acceleration and emission processes in their extreme energy limit. They are, however, out of reach for satellites but accessible to ground-based telescopes. Previous searches for pulsations in the VHE domain have resulted in the detection up to an energy ~ 1 TeV of only one pulsar, that associated with the Crab nebula [7–9], while providing stringent upper limits on the VHE fluxes of other pulsars [10, 11].

We report here on the detection of the Vela pulsar (hereafter Vela), PSR B0833–45, in the multi-TeV energy range with the H.E.S.S. array of five imaging atmospheric Cherenkov telescopes (CT1-5). H.E.S.S. is situated in the Khomas Highland of Namibia and operates in the tens of GeV to tens of TeV energy range. Vela was among the very first pulsars discovered at radio frequencies [12], the second one detected in > 30 MeV gamma rays [13], and stands out as being by far the brightest pulsar in these two domains. Located nearby, at a distance of 287 pc [14], it is a young pulsar with a spin period of 89 ms and a characteristic age of 11 kyr. In the GeV range, its rotation phase-folded gamma-ray light curve exhibits two peaks, labeled P1 and P2, separated by 0.43 in phase and connected by a bridge emission containing a third peak labeled P3 [5, 15]. Recently, using the largest H.E.S.S. telescope, CT5, which, thanks to its 28-m equivalent diameter provides a relatively low energy threshold, we detected the P2 pulse of Vela in the 10 – 80 GeV energy range and showed that there was compelling evidence that the bright GeV component has a cutoff at energies well below 100 GeV [15].

Results reported here are based on deeper observations (80 hours) above an energy threshold of 260 GeV, performed with the 12-m diameter CT1-4 telescopes during the 2004-2007 and 2014-2016 observing seasons [16]. Given the lack of *a priori* knowledge of the source spectral hardness (whether soft or hard, i.e. dominated by events with energy below ~ 1 TeV, or *vice versa*), the search for pulsations was conducted by applying periodicity tests on data sets selected using four predefined and increasing energy thresholds of 0.5, 1, 3 and 7 TeV. Three types of periodicity tests were used: the H-test [17] where no *a priori* knowledge of the light curve (or phasogram, i.e., the phase-folded distribution of events) is assumed, the C-test [18] where the position and the (approximate) width of the pulse shape are supposed to be known beforehand, and

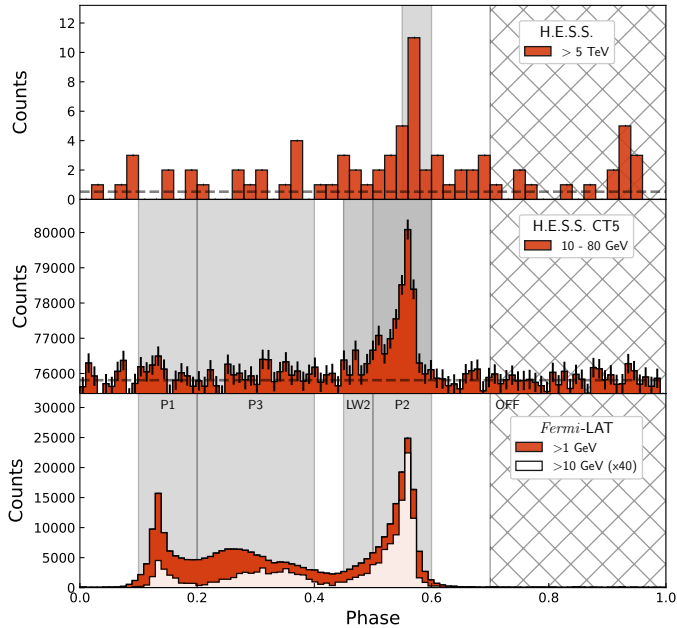


Fig. 1 Phasogram of Vela as measured with H.E.S.S. CT1-4 for energies above 5 TeV, with H.E.S.S. CT5 in the 10 – 80 GeV range and with the *Fermi*-LAT above 1 GeV and 10 GeV, respectively. Phase values are computed relative to the radio pulse. The ranges corresponding to different features in the pulse profile at low energies (<100 GeV) are shown as grey-colored intervals: pulses P1, P3, P2, and the leading wing of P2, LW2. The *off*-phase interval [0.7–1.0] is shown as a hatched area and the dashed line on the two upper panels shows the estimated level of the background [15]. The *Fermi*-LAT light curve for energies above 10 GeV has been multiplied by a factor 40 for better visibility.

a maximum likelihood-ratio (LR) test [19] based on *a priori* defined *On*- and *Off*-phase intervals. The pulse P2 of the Vela pulsar, dominating in the tens of GeV energy range, was considered as the prime candidate for detection in the VHE range and its parameters, as derived from the *Fermi*-LAT phasogram above 10 GeV [15], were used as input to the tests. Pulsed emission was detected at a statistical significance exceeding 4σ for all the tests: above energy thresholds of 1, 3 and 7 TeV with the C-test (4.3, 4.9 and 5.6σ , respectively), 3 and 7 TeV with the LR test (4.7 and 4.8σ , respectively), and above 7 TeV for the H-test (4.5σ). Posterior to this detection, we derived the significance of the pulsations above two other energy thresholds, 5 and 20 TeV. The signal displays its highest significance level above 5 TeV and is clearly detected above 20 TeV, with, e.g., C-test results of 5.8 and 4.6σ , respectively (Table S1).

Fig. 1 shows the phasogram of Vela obtained with and the *Fermi*-LAT. The sole significant feature present in the multi-TeV range lies at a peak position ($\phi_{P2}^{\text{TeV}} = 0.568 \pm 0.003$) that is statistically compatible with that of the P2 pulse observed in

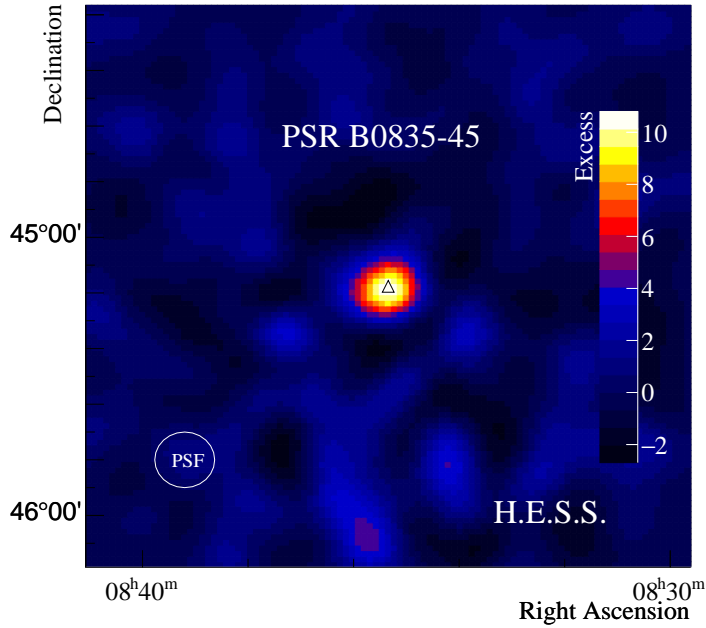


Fig. 2 Excess map of the P2 pulse of Vela as measured with H.E.S.S. for energies above 5 TeV. Gaussian-smoothed excess map ($\sigma = 0.15^\circ$) in the P2 phase range, where the *on* and *off* maps are made after selection of events in *on*- and *off*-phase intervals defined as $[0.55 - 0.6]$ and $[0.7 - 1.0]$, respectively. The triangle indicates the position of the pulsar and the circle shows the 1σ instrument point spread function.

the HE energy range ($\phi_{P2}^{\text{GeV}} = 0.565 \pm 0.001$). This pulsation also exhibits a similar width (e.g., FWHM) to that measured in the latter energy range. This, together with the fact that P1 disappears above few tens of GeV, is in line with the energy evolution of the light curve at GeV energies [16].

Fig. 2 shows the map of photons with energies above 5 TeV in the P2 pulse phase range. The spatial distribution of photons is centered on Vela and its spread is compatible with the H.E.S.S. point-spread function, as expected for a point-like source. The spectral energy distribution of the P2 pulse is shown in Fig. 3. It was measured by selecting signal and background events in the phase ranges of $[0.55 - 0.6]$ and $[0.7 - 1.0]$, respectively. The fit of a power-law function ($dN(E)/dE = \Phi_0 (E/E_0)^{-\Gamma_{\text{VHE}}}$) in the 260 GeV – 28.5 TeV energy range resulted in a very hard spectrum with photon index $\Gamma_{\text{VHE}} = 1.4 \pm 0.3^{\text{stat}} \pm 0.1^{\text{syst}}$, and normalization $\Phi_0 = (1.74 \pm 0.52^{\text{stat}} \pm 0.35^{\text{syst}}) \times 10^{-15} \text{ erg}^{-1} \text{ cm}^{-2} \text{ s}^{-1}$ at the reference energy $E_0 = 4.24 \text{ TeV}$, implying an isotropic luminosity $L_{20\text{TeV}} \simeq 2 \times 10^{30} \text{ erg s}^{-1}$. Given the steeply falling HE spectrum (photon index $\Gamma_{\text{HE}} = 5.25 \pm 0.25^{\text{stat}}$ [15]), and the non detection upper limits in the 100–660 GeV range, the extremely hard VHE spectrum can only be a distinct and new component.

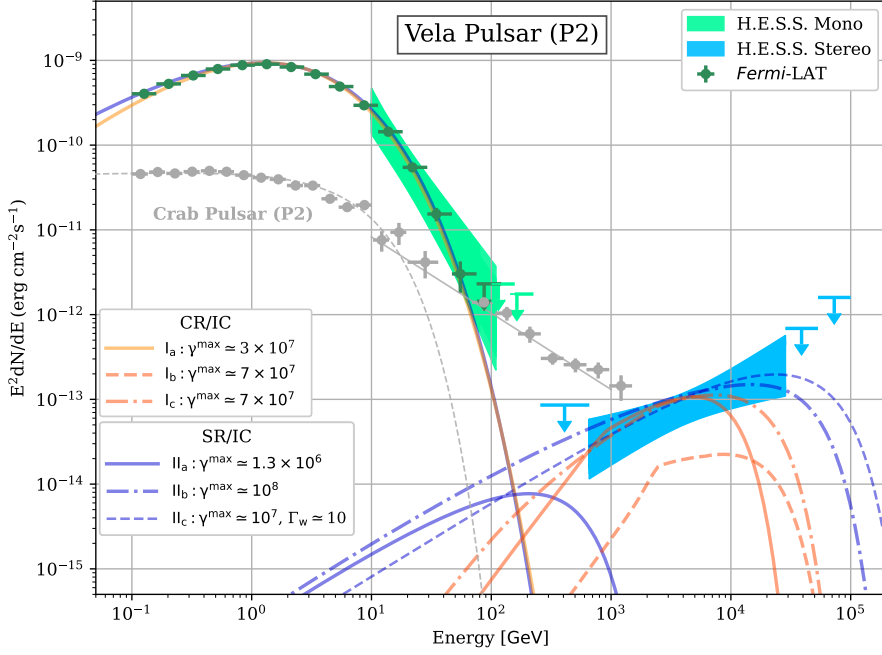


Fig. 3 Spectral energy distribution (SED) of the P2 pulse of Vela

Data: The green points and the green area below 100 GeV show the measurements by *Fermi*-LAT and by H.E.S.S. CT5 in monoscopic mode [15], respectively. The blue area and upper limits (ULs) above 260 GeV correspond to measurements with H.E.S.S. CT1-4 in stereoscopic mode (this work). All ULs are given at 99.7% confidence level, and both CT5 and CT1-4 uncertainty bands consist of 1σ confidence intervals combined with systematic errors on the H.E.S.S. energy scale. For comparison, the SED of the P2 pulse of the Crab pulsar as measured by *Fermi*-LAT and MAGIC [9] is also shown.

Heuristic spectral models: Either magnetospheric curvature radiation (CR) or synchrotron radiation (SR) in the wind zone is considered for emission below 100 GeV, while for the TeV range inverse-Compton (IC) scattering of soft photons is assumed (see illustration in Fig. 4 and [16]). The CR/IC and SR/IC schemes are shown in orange and blue colors, respectively. The H.E.S.S. data require $\gamma^{\max} \gtrsim 7 \times 10^7$ and hence exclude the traditional scenarios I_a (CR/IC), i.e. emission in the inner magnetosphere or at the light cylinder (LC), and II_a (SR/IC), where γ^{\max} is limited by SR cooling. The dashed and dash-dotted curves show possible paths to fit the data, including a Doppler-boosted scenario (II_c) with bulk wind Lorentz factor $\Gamma_w \simeq 10$ (see text). The IC intensity is only loosely constrained due to its strong dependence on model-dependent geometrical factors and on the density of putative target photons, which in turn depends on the unknown lower limit of its spectrum. All spectral models are computed with IC seed photons extending into the FIR domain (0.005 – 4 eV) and are normalized (for II_a, its extrapolation) to a level of $10^{-13} \text{ erg}^{-1} \text{ cm}^{-2} \text{ s}^{-1}$ at 5 TeV, except I_c. For the latter model, the targets are limited to the O-NIR range (0.1 – 4 eV). More sophisticated approaches in the CR/IC scenario are shown in Fig. M2.

The most likely process for producing gamma rays at multi-TeV energies by energetic electrons, whatever the acceleration mechanism and emission regions are, is inverse-Compton (IC) scattering of low-energy photons (e.g. [20–23]). Potential target photon fields in Vela may include the observed non-thermal X-rays [24, 25], thermal X-rays from the neutron star surface [25], UV [26], or optical [27, 28] to the near-infrared [29] emission (O-NIR). For all these photons IC scattering would proceed in the Klein-Nishina (K-N) regime. The O-NIR radiation field with its possible extension down to the far-infrared (FIR) domain constitutes the most plausible target [20–22, 30]. In the K-N regime, the maximum measured photon energy $E^{\max} \gtrsim 20$ TeV constrains the electron Lorentz factor to be $\gamma_{\text{IC}}^{\max} \gtrsim E^{\max}/m_e c^2 \gtrsim 4 \times 10^7$. The fact that P2 in Vela occurs at the same phase position for both spectral components, HE and VHE, suggests that these components are generated by the same population of electrons, but through different radiation processes. In the following we discuss the implications of the H.E.S.S. discovery under this hypothesis.

Several hypotheses have been proposed to describe the acceleration of electrons to ultra-relativistic energies (see illustration in Fig. 4). In a first scenario, particles are accelerated along the magnetic field lines in the pulsar magnetosphere by the (unscreened) electric field E_{\parallel} that is parallel to these local lines, in charge-depleted cavities (or gaps) [20, 31, 32] within the light cylinder (LC), or, as recently posited, also slightly beyond [33]. The latter is defined as the radius at which the co-rotation speed equals that of light in vacuum ($R_{\text{LC}} = cP/2\pi \simeq 4.3 \times 10^8$ cm for the Vela pulsar given its period $P=89.3$ ms). In a second scenario, acceleration takes place through magnetic reconnection in the equatorial current sheet (CS) of the striped wind beyond the LC [34–40]).

In the first scenario, curvature radiation (CR) is traditionally posited to explain the emission observed in the GeV range, e.g. [21, 41–43], and a combination of synchrotron (SR) and curvature (synchro-curvature radiation, SCR), to also reproduce the MeV to GeV spectral shape (e.g., [33, 44]). The maximum Lorentz factor of the electrons is limited by the magnitude of the accelerating electric field E_{\parallel} in the gap – or equivalently, the magnetic conversion efficiency $\eta = E_{\parallel}/B$ – and by CR losses which depend on the curvature radius ρ_c of particle trajectories. This limit can be expressed as $\gamma_{\text{CR}}^{\max} \propto \rho_c^{1/2} \eta^{1/4}$ [16]. The magnitude of η depends on the particular version of the acceleration gaps¹ with values usually assumed to be below 10% at the LC [33, 45]. Hence, to achieve the maximum photon energy observed by H.E.S.S., E^{\max} , large curvature radii $\rho_c \gtrsim 4 \times 10^8$ cm $\approx R_{\text{LC}}$ are required [16]. Taking into account the HE and VHE spectra provides further constraints. The HE spectral peak lying at $E_{\text{HE}}^{\text{peak}} \simeq 1.5$ GeV [5, 6, 15] depends also on the combination of η and ρ_c as $E_{\text{HE}}^{\text{peak}} \propto \rho_c^{1/2} \eta^{3/4}$. Considering first an emission zone close to the LC, where $\rho_c \sim R_{\text{LC}}$, and fitting the GeV component alone results in $\gamma_{\text{CR}}^{\max} \simeq 3 \times 10^7$ and $\eta \simeq 0.02$ which is insufficient to reproduce the TeV data (curve I_a in Fig. 3). A joint fit of both components requires $\gamma_{\text{IC}}^{\max} \gtrsim 7 \times 10^7$, and by identifying $\gamma_{\text{IC}}^{\max}$ with $\gamma_{\text{CR}}^{\max}$ we obtain $\eta \ll 0.1$ and $\rho_c \gg R_{\text{LC}}$ (curve I_b in Fig. 3, red curve in Fig. M1). Hence, if the HE and VHE

¹And may vary with altitude above the pulsar surface.

components are produced by the same electron population, the H.E.S.S. data constrain the emission regions to lie beyond the LC and imply at the same time a low magnetic conversion efficiency.

In the second scenario, SR has been proposed as the mechanism responsible for the GeV radiation [37, 40, 46, 47], and applied to model the HE component of the Crab and Vela pulsars [48, 49]. Hard particle spectra reaching maximum energies beyond the radiative cooling limit are expected in the magnetic reconnection scheme [50], due to a two-step process: the acceleration takes place deep in the CS where the magnitude of the perpendicular B is weak, and is followed by abrupt SR cooling in the magnetic loops (plasmoids) where B-field is strong (e.g., [51–55]). The sharp HE cutoffs observed at a few GeV in the spectra of pulsars are attributed to the latter step. In the Vela case, the SR cutoff would correspond to a maximum Lorentz factor of $\gamma_{\text{SR}}^{\text{max}} \simeq 1.3 \times 10^6$ [16]. The matching inferred particle spectral indices in the sub-GeV and TeV regimes, and the compatible luminosity levels when considering the available photon fields [16], renders the SR/IC scenario in the dissipation region near the LC [55] attractive. However, $\gamma_{\text{SR}}^{\text{max}}$ is two orders of magnitude lower than the one derived from the H.E.S.S. data (curve II_a in Fig. 3) and requires a more complex approach. One can speculate on the escape of the highest energy (and IC-emitting) particles from plasmoids, or their re-energization after SR cooling [55–57], or alternatively, assume that two populations of electrons are responsible for the HE and VHE components [16] (curve II_b in Fig. 3). Invoking a Doppler-boosted plasma as the origin of the GeV and/or multi-TeV emission [23, 46, 48, 49, 58–60] alleviates the tensions related to the maximum achievable energy in the SR/IC scheme. The *Fermi*-LAT and H.E.S.S. data can be used to constrain the wind Lorentz factor to be $\Gamma_w \gtrsim 5$ at a distance of $\simeq 5R_{\text{LC}}$ where the gamma-ray emission region should be located (curve II_b in Fig. 3). This region is, however, further than the typical zone at $\sim 1 - 2R_{\text{LC}}$ where the dissipation of the energy is believed to occur through SR according to current Particle-in-cell (PIC) simulations [55]. Resorting to differentiated SR and IC cooling zones could mitigate this issue with the condition that the photons from these zones are beamed into similar phases.

Reproducing the HE-VHE light curves poses indeed further challenges. As mentioned above, the TeV light curve maintains the trend observed below 80 GeV, where the ratio of the intensities of the two peaks P1 and P2 decreases with energy (see Fig. 1 and [2, 6]), that is, the cutoff energy of the P2 spectrum is higher than that of P1. To form the light curves as measured in the HE and VHE domains, gamma-ray photons should originate in radially extended and properly shaped zones. Special-relativistic effects and the B -field structure arrange the photons to arrive at Earth at similar phases, i.e., to form caustics. Within (or slightly beyond) the magnetosphere, these caustics arise naturally [61–66], and the higher cutoff energies of the P2 spectral component can be attributed to larger curvature radii of the orbits of electrons responsible for P2 via CR [67, 68]. Caustics can also form within the equatorial CS in the near wind zone [46, 53, 69], resulting in double-peaked light curves with specific predictions for the polarization of the HE emission [70]. Alternatively, the phase coherence of the pulsations can be obtained by a relativistic beaming effect in the far wind zone [37–40]. In this case, the higher cutoff energy of the P2 pulse could arise from the difference in

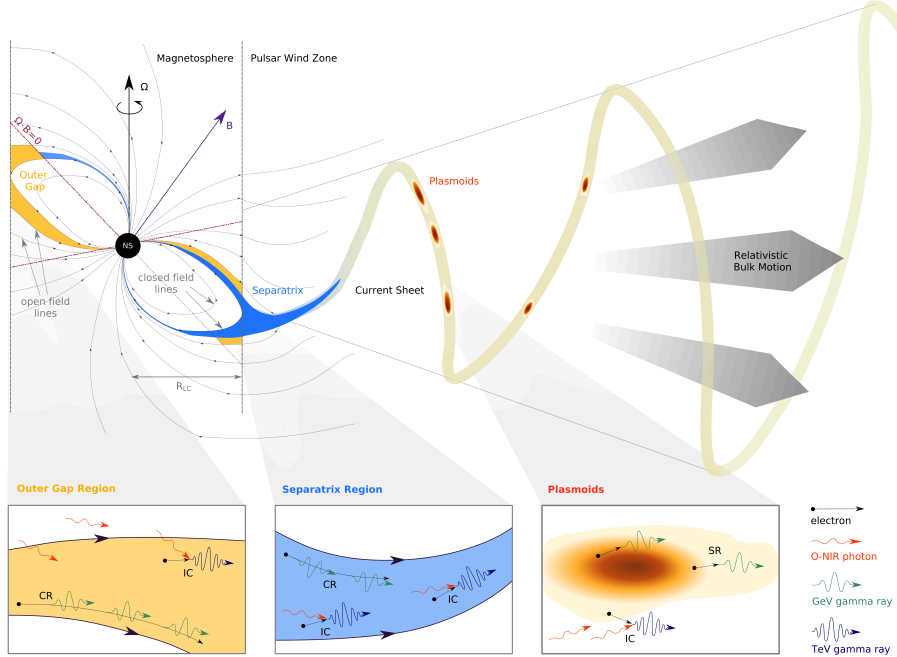


Fig. 4 Sketch illustrating main scenarios of particle acceleration and gamma-ray emission. Electrons are accelerated either (i) along magnetic field lines in charge-depleted cavities within the light cylinder (LC), i.e. outer gaps, or slightly beyond, i.e. the separatrix/current sheet model, or (ii) through magnetic reconnection in the equatorial current sheet of the striped wind beyond the LC. GeV gamma rays are either due to curvature radiation (CR) or synchrotron radiation (SR), while TeV photons are produced through inverse-Compton (IC) scattering of low-energy (O-NIR) photons (see text). For sake of readability scales are not respected: the pulsar size is exaggerated as well as the size of the acceleration and emission zones. The neutron star (NS) has a diameter of ~ 12 km and the light-cylinder radius $R_{LC} \simeq 4300$ km. The wavelength of the current sheet stripes ($2 \times \pi \times R_{LC}$) is twice as large as that depicted in the sketch.

the maximum energies attained by the positron and electron populations with potentially distinct contributions to the pulses [53, 69]. However, as discussed above, both CR/IC and SR/IC scenarios are strongly challenged by the H.E.S.S. measurements.

The results reported here establish Vela as the first pulsating source of tens of TeV gamma rays and as the second pulsar detected in the VHE range, after the Crab pulsar [9]. We find the dominant dissipation of energy, and thus particle acceleration and photon emission, to happen beyond the pulsar LC or at its periphery, and we set a lower limit of $4 \times 10^7 m_e c^2$ to the maximum achievable electron energy. In contrast to the Crab pulsar, of which the hardest pulsation is shown in Fig. 3, Vela unambiguously displays a new spectral component, with a very hard index, extending to energies an order of magnitude higher. These are unprecedented challenges to the state-of-the-art models of HE and VHE emission from pulsars.

Our discovery opens a new observation window for detection of other pulsars in the TeV to the tens of TeV range with current and upcoming more sensitive instruments such as LHAASO [71] or CTA [72]. It paves the path for a better understanding of these positron factories in the Galaxy, and their potential contribution to the local positron excess above 10 GeV as well as to Ultra-High-Energy cosmic rays. The hard radiation component is also a new tool for probing the role of magnetic reconnection as an acceleration process in isolated pulsars, with possible implications for other highly magnetised plasma in diverse astrophysical contexts., e.g., black hole magnetospheres and jet-accretion disc systems.

References

- [1] Manchester, R. N., Hobbs, G. B., Teoh, A. & Hobbs, M. The Australia Telescope National Facility Pulsar Catalogue. *AJ* **129**, 1993–2006 (2005).
- [2] Abdo, A. A. *et al.* The Second Fermi Large Area Telescope Catalog of Gamma-Ray Pulsars. *ApJS* **208**, 17 (2013).
- [3] Kanbach, G. *et al.* EGRET observations of the VELA pulsar, PSR0833-45. *A&A* **289**, 855–867 (1994).
- [4] Nolan, P. L. *et al.* EGRET observations of pulsars. *A&AS* **120**, 61–64 (1996).
- [5] Abdo, A. A. *et al.* Fermi Large Area Telescope Observations of the Vela Pulsar. *ApJ* **696**, 1084–1093 (2009).
- [6] Abdo, A. A., Ackermann, M., Ajello, M. & Allafort, A. e. a. The Vela Pulsar: Results from the First Year of Fermi LAT Observations. *ApJ* **713**, 154–165 (2010).
- [7] VERITAS Collaboration *et al.* Detection of Pulsed Gamma Rays Above 100 GeV from the Crab Pulsar. *Science* **334**, 69 (2011).
- [8] Aleksić, J. *et al.* Phase-resolved energy spectra of the Crab pulsar in the range of 50–400 GeV measured with the MAGIC telescopes. *A&A* **540**, A69 (2012).
- [9] Ansoldi, S. *et al.* Teraelectronvolt pulsed emission from the Crab Pulsar detected by MAGIC. *A&A* **585**, A133 (2016).
- [10] Aharonian, F. *et al.* Search for pulsed VHE gamma-ray emission from young pulsars with HESS. *A&A* **466**, 543–554 (2007).
- [11] Archer, A. *et al.* A Search for Pulsed Very High-energy Gamma-Rays from 13 Young Pulsars in Archival VERITAS Data. *ApJ* **876**, 95 (2019).
- [12] Large, M. I., Vaughan, A. E. & Mills, B. Y. A Pulsar Supernova Association? *Nature* **220**, 340–341 (1968).

- [13] Thompson, D. J., Fichtel, C. E., Kniffen, D. A. & Ogelman, H. B. SAS-2 high-energy gamma-ray observations of the VELA pulsar. *ApJ* **200**, L79–L82 (1975).
- [14] Dodson, R., Legge, D., Reynolds, J. E. & McCulloch, P. M. The Vela Pulsar’s Proper Motion and Parallax Derived from VLBI Observations. *ApJ* **596**, 1137–1141 (2003).
- [15] H. E. S. S. Collaboration *et al.* First ground-based measurement of sub-20 GeV to 100 GeV γ -Rays from the Vela pulsar with H.E.S.S. II. *A&A* **620**, A66 (2018).
- [16] Further details are available in the Methods section.
- [17] de Jager, O. C., Raubenheimer, B. C. & Swanepoel, J. W. H. A powerful test for weak periodic signals with unknown light curve shape in sparse data. *A&A* **221**, 180–190 (1989).
- [18] de Jager, O. C. On Periodicity Tests and Flux Limit Calculations for Gamma-Ray Pulsars. *ApJ* **436**, 239 (1994).
- [19] Li, T.-P. & Ma, Y.-Q. Analysis methods for results in gamma-ray astronomy. *ApJ* **272**, 317–324 (1983).
- [20] Cheng, K. S., Ho, C. & Ruderman, M. Energetic radiation from rapidly spinning pulsars. I - Outer magnetosphere gaps. II - VELA and Crab. *ApJ* **300**, 500–539 (1986).
- [21] Romani, R. W. Gamma-Ray Pulsars: Radiation Processes in the Outer Magnetosphere. *ApJ* **470**, 469 (1996).
- [22] Hirotani, K. Gamma-Ray Emissions from Pulsars: Spectra of the TEV Fluxes from Outer Gap Accelerators. *ApJ* **549**, 495–508 (2001).
- [23] Bogovalov, S. V. & Aharonian, F. A. Very-high-energy gamma radiation associated with the unshocked wind of the Crab pulsar. *MNRAS* **313**, 504–514 (2000).
- [24] Harding, A. K. *et al.* The Multicomponent Nature of the Vela Pulsar Nonthermal X-Ray Spectrum. *ApJ* **576**, 376–380 (2002).
- [25] Manzali, A., De Luca, A. & Caraveo, P. A. Phase-resolved Spectroscopy of the Vela Pulsar with XMM-Newton. *ApJ* **669**, 570–578 (2007).
- [26] Romani, R. W., Kargaltsev, O. & Pavlov, G. G. The Vela Pulsar in the Ultraviolet. *ApJ* **627**, 383–389 (2005).
- [27] Mignani, R. P., Zharikov, S. & Caraveo, P. A. The optical spectrum of the Vela pulsar. *A&A* **473**, 891–896 (2007).

- [28] Spolon, A. *et al.* Timing analysis and pulse profile of the Vela pulsar in the optical band from Iqueye observations. *MNRAS* **482**, 175–183 (2019).
- [29] Zyuzin, D., Shibano, Y., Danilenko, A., Mennickent, R. E. & Zharikov, S. The Vela Pulsar and Its Likely Counter-jet in the K_s Band. *ApJ* **775**, 101 (2013).
- [30] Aharonian, F. A. & Bogovalov, S. V. Exploring physics of rotation powered pulsars with sub-10 GeV imaging atmospheric Cherenkov telescopes. *New A* **8**, 85–103 (2003).
- [31] Arons, J. & Scharlemann, E. T. Pair formation above pulsar polar caps: structure of the low altitude acceleration zone. *ApJ* **231**, 854–879 (1979).
- [32] Muslimov, A. G. & Harding, A. K. Extended Acceleration in Slot Gaps and Pulsar High-Energy Emission. *ApJ* **588**, 430–440 (2003).
- [33] Harding, A. K., Kalapotharakos, C., Barnard, M. & Venter, C. Multi-TeV Emission from the Vela Pulsar. *ApJ* **869**, L18 (2018).
- [34] Michel, F. C. Coherent Neutral Sheet Radiation from Pulsars. *Comments on Astrophysics and Space Physics* **3**, 80 (1971).
- [35] Coroniti, F. V. Magnetically Striped Relativistic Magnetohydrodynamic Winds: The Crab Nebula Revisited. *ApJ* **349**, 538 (1990).
- [36] Michel, F. C. Magnetic Structure of Pulsar Winds. *ApJ* **431**, 397 (1994).
- [37] Lyubarskii, Y. E. A model for the energetic emission from pulsars. *A&A* **311**, 172–178 (1996).
- [38] Kirk, J. G. & Lyubarsky, D. Y. Reconnection in Pulsar Winds. *PASA* **18**, 415–420 (2001).
- [39] Kirk, J. G., Skjæraasen, O. & Gallant, Y. A. Pulsed radiation from neutron star winds. *A&A* **388**, L29–L32 (2002).
- [40] Pétri, J. High-energy emission from the pulsar striped wind: a synchrotron model for gamma-ray pulsars. *MNRAS* **424**, 2023–2027 (2012).
- [41] Takata, J., Shibata, S., Hirokuni, K. & Chang, H. K. A two-dimensional electro-dynamical outer gap model for γ -ray pulsars: γ -ray spectrum. *MNRAS* **366**, 1310–1328 (2006).
- [42] Hirokuni, K. Outer-Gap versus Slot-Gap Models for Pulsar High-Energy Emissions: The Case of the Crab Pulsar. *ApJ* **688**, L25 (2008).
- [43] Takata, J., Ng, C. W. & Cheng, K. S. Probing gamma-ray emissions of Fermi-LAT pulsars with a non-stationary outer gap model. *MNRAS* **455**, 4249–4266

- (2016).
- [44] Viganò, D. & Torres, D. F. Modelling of the γ -ray pulsed spectra of Geminga, Crab, and Vela with synchro-curvature radiation. *MNRAS* **449**, 3755–3765 (2015).
 - [45] Hirotani, K. Particle Accelerator in Pulsar Magnetospheres: Super-Goldreich-Julian Current with Ion Emission from the Neutron Star Surface. *ApJ* **652**, 1475–1493 (2006).
 - [46] Arka, I. & Dubus, G. Pulsed high-energy γ -rays from thermal populations in the current sheets of pulsar winds. *A&A* **550**, A101 (2013).
 - [47] Cerutti, B. & Philippov, A. A. Dissipation of the striped pulsar wind. *A&A* **607**, A134 (2017).
 - [48] Mochol, I. & Pétri, J. Very high energy emission as a probe of relativistic magnetic reconnection in pulsar winds. *MNRAS* **449**, L51–L55 (2015).
 - [49] Mochol, I. Torres, D. F. (ed.) *Pulsar Striped Winds*. (ed. Torres, D. F.) *Modelling Pulsar Wind Nebulae*, Vol. 446 of *Astrophysics and Space Science Library*, Springer, 135–159 (2017). [1702.00720](#).
 - [50] Kirk, J. G. Particle Acceleration in Relativistic Current Sheets. *Phys. Rev. Lett.* **92**, 181101 (2004).
 - [51] Uzdensky, D. A., Cerutti, B. & Begelman, M. C. Reconnection-powered Linear Accelerator and Gamma-Ray Flares in the Crab Nebula. *ApJ* **737**, L40 (2011).
 - [52] Werner, G. R., Uzdensky, D. A., Cerutti, B., Nalewajko, K. & Begelman, M. C. The Extent of Power-law Energy Spectra in Collisionless Relativistic Magnetic Reconnection in Pair Plasmas. *ApJ* **816**, L8 (2016).
 - [53] Cerutti, B., Philippov, A. A. & Spitkovsky, A. Modelling high-energy pulsar light curves from first principles. *MNRAS* **457**, 2401–2414 (2016).
 - [54] Werner, G. R. & Uzdensky, D. A. Nonthermal Particle Acceleration in 3D Relativistic Magnetic Reconnection in Pair Plasma. *ApJ* **843**, L27 (2017).
 - [55] Cerutti, B., Philippov, A. A. & Dubus, G. Dissipation of the striped pulsar wind and non-thermal particle acceleration: 3D PIC simulations. *A&A* **642**, A204 (2020).
 - [56] Petropoulou, M. & Sironi, L. The steady growth of the high-energy spectral cut-off in relativistic magnetic reconnection. *MNRAS* **481**, 5687–5701 (2018).
 - [57] Hakobyan, H., Philippov, A. & Spitkovsky, A. Effects of Synchrotron Cooling and Pair Production on Collisionless Relativistic Reconnection. *ApJ* **877**, 53 (2019).

- [58] Aharonian, F. A., Bogovalov, S. V. & Khangulyan, D. Abrupt acceleration of a ‘cold’ ultrarelativistic wind from the Crab pulsar. *Nature* **482**, 507–509 (2012).
- [59] Tavernier, T. *A quest for the emission of the Vela pulsar at very high energies: observation, detection, and study from GeV to TeV with the Fermi satellite and the H.E.S.S. Cherenkov imaging telescopes*. Ph.D. thesis, University of Paris 7, APC (2015).
- [60] Spir-Jacob, M. *Observation and detection of pulsars with the H.E.S.S. gamma-ray telescopes, and phenomenology of a new pulsed spectral component reaching 20 TeV*. Ph.D. thesis, University of Paris 7, APC (2019).
- [61] Morini, M. Inverse Compton gamma-rays from pulsars. I. The VELA pulsar. *MNRAS* **202**, 495–510 (1983).
- [62] Romani, R. W. & Yadigaroglu, I. A. Gamma-Ray Pulsars: Emission Zones and Viewing Geometries. *ApJ* **438**, 314 (1995).
- [63] Cheng, K. S., Ruderman, M. & Zhang, L. A Three-dimensional Outer Magnetospheric Gap Model for Gamma-Ray Pulsars: Geometry, Pair Production, Emission Morphologies, and Phase-resolved Spectra. *ApJ* **537**, 964–976 (2000).
- [64] Dyks, J. & Rudak, B. Two-Pole Caustic Model for High-Energy Light Curves of Pulsars. *ApJ* **598**, 1201–1206 (2003).
- [65] Dyks, J., Harding, A. K. & Rudak, B. Relativistic Effects and Polarization in Three High-Energy Pulsar Models. *ApJ* **606**, 1125–1142 (2004).
- [66] Bai, X.-N. & Spitkovsky, A. Uncertainties of Modeling Gamma-ray Pulsar Light Curves Using Vacuum Dipole Magnetic Field. *ApJ* **715**, 1270–1281 (2010).
- [67] Harding, A. K., Venter, C. & Kalapotharakos, C. Very-high-energy Emission from Pulsars. *ApJ* **923**, 194 (2021).
- [68] Barnard, M., Venter, C., Harding, A. K., Kalapotharakos, C. & Johnson, T. J. Probing the High-energy Gamma-Ray Emission Mechanism in the Vela Pulsar via Phase-resolved Spectral and Energy-dependent Light-curve Modeling. *ApJ* **925**, 184 (2022).
- [69] Philippov, A. A. & Spitkovsky, A. Ab-initio Pulsar Magnetosphere: Particle Acceleration in Oblique Rotators and High-energy Emission Modeling. *ApJ* **855**, 94 (2018).
- [70] Cerutti, B., Mortier, J. & Philippov, A. A. Polarized synchrotron emission from the equatorial current sheet in gamma-ray pulsars. *MNRAS* **463**, L89–L93 (2016).
- [71] Aharonian, F. *et al.* Prospects for a multi-TeV gamma-ray sky survey with the LHAASO water Cherenkov detector array. *Chinese Physics C* **44**, 065001 (2020).

- [72] Acharya, B. S. *et al.* Introducing the CTA concept. *Astropart. Phys.* **43**, 3–18 (2013).
- [73] Astropy Collaboration *et al.* Astropy: A community Python package for astronomy. *A&A* **558**, A33 (2013).
- [74] Zabalza, V. Naima: a python package for inference of particle distribution properties from nonthermal spectra. *Proceedings of the 34th International Cosmic Ray Conference, 30 July - 6 August, 2015. The Hague, The Netherlands.* 922–930 (2015).
- [75] Aharonian, F. *et al.* Observations of the Crab nebula with HESS. *A&A* **457**, 899–915 (2006).
- [76] Hofmann, W. *et al.* Comparison of techniques to reconstruct VHE gamma-ray showers from multiple stereoscopic Cherenkov images. *Astropart. Phys.* **12**, 135–143 (1999).
- [77] Becherini, Y., Djannati-Ataï, A., Marandon, V., Punch, M. & Pita, S. A new analysis strategy for detection of faint γ -ray sources with Imaging Atmospheric Cherenkov Telescopes. *Astropart. Phys.* **34**, 858–870 (2011).
- [78] Hoecker, A. *et al.* TMVA - Toolkit for Multivariate Data Analysis. *arXiv e-prints physics/0703039* (2007).
- [79] Bernlöhner, K. Simulation of imaging atmospheric Cherenkov telescopes with CORSIKA and sim_telarray. *Astropart. Phys.* **30**, 149–158 (2008).
- [80] de Naurois, M. & Rolland, L. A high performance likelihood reconstruction of γ -rays for imaging atmospheric Cherenkov telescopes. *Astropart. Phys.* **32**, 231–252 (2009).
- [81] Ohm, S., van Eldik, C. & Egberts, K. γ /hadron separation in very-high-energy γ -ray astronomy using a multivariate analysis method. *Astropart. Phys.* **31**, 383–391 (2009). URL <http://www.sciencedirect.com/science/article/pii/S0927650509000589>.
- [82] Parsons, R. D. & Hinton, J. A. A monte carlo template based analysis for air-cherenkov arrays. *Astropart. Phys.* **56**, 26–34 (2014). URL <http://www.sciencedirect.com/science/article/pii/S0927650514000231>.
- [83] Funk, S. *et al.* The trigger system of the H.E.S.S. telescope array. *Astropart. Phys.* **22**, 285–296 (2004).
- [84] Hobbs, G. B., Edwards, R. T. & Manchester, R. N. TEMPO2, a new pulsar-timing package - I. An overview. *MNRAS* **369**, 655–672 (2006).

- [85] Palfreyman, J., Dickey, J. M., Hotan, A., Ellingsen, S. & van Straten, W. Alteration of the magnetosphere of the Vela pulsar during a glitch. *Nature* **556**, 219–222 (2018).
- [86] Piron, F. *et al.* Temporal and spectral gamma-ray properties of JASTROBJ Mkn 421/ASTROBJ above 250 GeV from CAT observations between 1996 and 2000. *A&A* **374**, 895–906 (2001).
- [87] Rudak, B. & Dyks, J. *The modeling of the Vela pulsar pulses - from optical to hard gamma-ray energy*, Vol. 301 of *International Cosmic Ray Conference*, 680 (2017). [1708.01556](#).
- [88] Hirovani, K. Luminosity Evolution of Gamma-Ray Pulsars. *ApJ* **766**, 98 (2013).
- [89] Blumenthal, G. R. & Gould, R. J. Bremsstrahlung, Synchrotron Radiation, and Compton Scattering of High-Energy Electrons Traversing Dilute Gases. *Rev. Mod. Phys.* **42**, 237–271 (1970).
- [90] Venter, C. & De Jager, O. C. Accelerating High-energy Pulsar Radiation Codes. *ApJ* **725**, 1903–1909 (2010).
- [91] Djannati-Ataï, A. *et al.* *H.E.S.S. stereoscopic observations of the Vela pulsar above 100 GeV*, 29th Texas Symposium on Relativistic Astrophysics (2017).
- [92] Cerutti, B., Werner, G. R., Uzdensky, D. A. & Begelman, M. C. Simulations of Particle Acceleration beyond the Classical Synchrotron Burnoff Limit in Magnetic Reconnection: An Explanation of the Crab Flares. *ApJ* **770**, 147 (2013).
- [93] Sironi, L. & Spitkovsky, A. Relativistic Reconnection: An Efficient Source of Non-thermal Particles. *ApJ* **783**, L21 (2014).

Acknowledgments

The support of the Namibian authorities and of the University of Namibia in facilitating the construction and operation of H.E.S.S. is gratefully acknowledged, as is the support by the German Ministry for Education and Research (BMBF), the Max Planck Society, the German Research Foundation (DFG), the Helmholtz Association, the Alexander von Humboldt Foundation, the French Ministry of Higher Education, Research and Innovation, the Centre National de la Recherche Scientifique (CNRS/IN2P3 and CNRS/INSU), the Commissariat à l'énergie atomique et aux énergies alternatives (CEA), the U.K. Science and Technology Facilities Council (STFC), the Irish Research Council (IRC) and the Science Foundation Ireland (SFI), the Knut and Alice Wallenberg Foundation, the Polish Ministry of Education and Science, agreement no. 2021/WK/06, the South African Department of Science and Technology and National Research Foundation, the National Commission on Research,

Science & Technology of Namibia (NCRST), the Austrian Federal Ministry of Education, Science and Research and the Austrian Science Fund (FWF), the Australian Research Council (ARC), the Japan Society for the Promotion of Science, the University of Amsterdam and the Science Committee of Armenia grant 21AG-1C085. Work at NRL is supported by NASA.

We appreciate the excellent work of the technical support staff in Berlin, Zeuthen, Heidelberg, Palaiseau, Paris, Saclay, Tübingen and in Namibia in the construction and operation of the equipment. This work benefited from services provided by the H.E.S.S. Virtual Organization, supported by the national resource providers of the EGI Federation. This research made use of the Python packages Astropy [73] and naima [74]. A. Djannati-Ataï thanks Benoît Cerutti and Jérôme Pétri for fruitful discussions on the striped-wind model during the “Entretiens sur l’observation et la modélisation des pulsars” sessions funded by the Programme National Hautes Energies (PNHE) of which the support is acknowledged here. The authors wish to acknowledge the seminal role played by our late colleague, Okkie de Jager, in opening up the VHE pulsar window of research.

Author Contributions Statement

A. Djannati-Ataï led the H.E.S.S. project of the Vela pulsar and the main H.E.S.S. data analysis. G. Giavitto and L. Mohrmann performed the cross-check analyses used in this study along with V. Marandon. The statistical assessment of the results relies on Monte Carlo simulations performed by M. Spir-Jacob. A. Djannati-Ataï developed the interpretation and modelling together with B. Rudak, M. Spir-Jacob, T. Tavernier, E. de Ona Wilhelmi and C. Venter. The manuscript was prepared by A. Djannati-Ataï, B. Rudak, E. de Ona Wilhelmi, C. Venter, and L. Mohrmann. T. Lohse and M. Böttcher supervised the review and discussion of the manuscript among the coauthors. The sketch in Fig. 4 was designed by H. Prokoph together with E. de Ona Wilhelmi, based on an initial proposal by M. Spir-Jacob and A. Djannati-Ataï. The other coauthors contributed by preparing and obtaining the observations, calibrating the data, simulating showers and developing analyses, developing, constructing, operating, and maintaining telescopes, cameras, and calibration devices, conducting data handling, data reduction and data analysis software. The ephemeris used for phase-folding the H.E.S.S. data was provided by M. Kerr, S. Johnston, R.M. Shannon and D. Smith. All authors meet the journal’s authorship criteria and have reviewed, discussed, and commented on the results and the manuscript.

Ethics declarations

The authors declare that they have no competing interests.

Data and Materials Availability

The H.E.S.S. raw data and the code used in this study are not public but belong to the H.E.S.S. collaboration. The high level data for the light curve (cf. Fig. 1), and the confidence interval for the spectral energy distributions (cf. Fig. 3) are available at: https://www.mpi-hd.mpg.de/hfm/HESS/pages/publications/auxiliary/2023_Vela_MultiTeV.

Methods

H.E.S.S. Observations and Data Analysis

Observations of the Vela pulsar were performed with the H.E.S.S. array of imaging Cherenkov telescopes, located in the Khomas Highland of Namibia ($23^{\circ}16'18''$ S, $16^{\circ}30'00''$ E, 1800 m). The H.E.S.S. array has been designed for the detection of high-energy (HE) and very-high-energy (VHE) gamma rays in the 10 GeV-100 TeV range. It consists of four imaging atmospheric Cherenkov telescopes (CT1-4), each having a 108 m^2 mirror area, placed in a square formation with a side length of 120 m, and a fifth telescope (CT5) with a larger mirror area of 614 m^2 placed at the center. The latter telescope was added in 2012 to extend the energy range of the array to below 100 GeV. The observations used for this study focused on the highest energy events and were performed in stereoscopic mode with CT1-4. Our first set of gamma-ray observations of the Vela pulsar with CT1-4 consisted of 16.3 hours and resulted in upper limits above a threshold energy of 170 GeV[10].

A total of 80 hours of data from 2004 to 2016 observing seasons were selected based on weather conditions and the instrumental status. Observations were mostly performed in wobble mode [75] with a source-to-center distance of 0.7° , and with the zenith angle ranging between 20° and 40° . When penetrating the atmosphere, gamma rays as well as charged cosmic rays interact with its constituents, producing showers of ultra-relativistic particles that emit Cherenkov light along their path in the air. The light collected by each dish forms an image of this shower and is recorded by highly sensitive cameras consisting of photo-tubes and fast electronics. The data analysis starts with the reconstruction of the direction and the virtual impact point on the

ground of each event, derived from the combination of information in shower images recorded by the camera of each telescope [75, 76]. The energy of each event and the discrimination parameters used to reject the background of charged cosmic rays that remain after a spatial (angular) cut at the 68% containment radius of the instrument, are obtained via a multi-variate analysis [77] based on a boosted decision tree (BDT) classifier implemented within the TMVA package [78]. The BDT is trained using extensive Monte Carlo (MC) simulations of γ -ray induced images [79] and real *off*-source data as signal and background inputs, respectively. The results presented in this paper were cross-checked with an alternative calibration, and with two additional analysis chains for the reconstruction and background suppression [80–82].

Timing and Phase Selection

The arrival time of each event is provided by a GPS receiver in the central trigger system of H.E.S.S. and is then software-corrected for the time delays in the array. A long-term stability of better than $2 \mu\text{s}$ is achieved for the system [83]. The pulsar phase corresponding to the arrival time of each event is calculated using the TEMPO2 package [84]. Event arrival times provided by a GPS receiver in the central trigger system of H.E.S.S. are transformed to the solar system barycentre where the pulsar phase of each event is computed using an ephemeris derived from radio data from the Parkes Radio Telescope. The ephemeris consisted of two overlapping solutions, valid for the ranges MJD 51602.43-56555.73 and 54175.52-57624.20 (with fiducial phase references, TZRMD = 54091.726 and 55896.55), with a precision of a few milli-periods ($100 - 300 \mu\text{s}$). Vela is known for its recurrent glitches. The two timing solutions are phase-connected and take properly into account the 3 glitches recorded in the years from 2004 to 2013 at

MJD 53193, 53960 and 55408.8. None of these glitches took place during an observation run and the glitch at MJD 57734.5 (December 12, 2016, studied in detail in [85]) lies beyond the H.E.S.S. 2016 observing period which ended at MJD 57541.7 (June 2, 2016).

Periodicity Search

The search for pulsations was conducted at four predefined and increasing energy thresholds of 0.5, 1, 3 and 7 TeV. These energies were intended to cover the plausible range of the source spectrum hardness (from soft to hard), given the absence of an *a priori* knowledge of it. Three types of periodicity tests were used: the H-test [17] where no *a priori* knowledge of the light curve (or phasogram, i.e., the phase-folded distribution of events) is assumed, the C-test [18] where the position and the (approximate) width of the pulse shape are supposed to be known beforehand, and a maximum likelihood-ratio (LR) test [19] based on *a priori* defined *On-* and *Off-*phase intervals. The pulse P2 of the Vela pulsar, dominating in the tens of GeV energy range, was considered and its parameters were derived from the *Fermi*-LAT phasogram above 10 GeV [15], i.e., $\phi_{P2}^{\text{GeV}} = 0.565$, and $w = 0.025$ (FWHM). The *Fermi*-LAT phasogram above 10 GeV was also used to define the *On-* and *Off-*phase intervals as [0.55,0.6] and [0.7,1.0], respectively.

The pulsed nature of the signal enables one to extract the *On-* and *Off-*source events from the same portion of the field of view, thereby eliminating one of the main sources of systematic effects arising from variations of acceptance as a function of direction in the sky and/or position in the camera. The required minimal significance level for detection of pulsations is consequently defined as 4σ , i.e., lower than that usually used for a DC (i.e. unpulsed) signal (5σ). Given the small number of events, the

probability distribution function of all tests was computed numerically using extensive MC simulations [60].

The periodicity test results are given in Table M1. The C-test resulted in trials-corrected (pre-trials) significance levels of 4.9σ (5.4σ) and 5.6σ (6.0σ) above energy thresholds of 3 and 7 TeV, respectively. For these thresholds, the corresponding H-test results are 3.9σ (4.5σ) and 4.5σ (5.0σ), while the likelihood-ratio test yielded post-trial significance levels of 4.7σ and 4.8σ , with excess counts of 18.2 and 14.3 events, respectively. The total number of trials is conservatively assumed to be equal to 12 and corresponds to the number of tests for periodicity (i.e. 3: the C-test, H-test and the likelihood-ratio test) applied to the data multiplied by the number of data sets (i.e. 4 sets corresponding to the 4 energy thresholds used for selection of events)². Lower post-trial significance levels were obtained for the data sets with energy thresholds of 0.5 TeV and 1 TeV, e.g., for the C-test, 3.7σ and 4.3σ , respectively, pointing to a hard energy spectrum at P2. Additional post-detection C-tests (likelihood-ratio tests) were performed above energy thresholds of 5 and 20 TeV. They resulted in significance levels of 5.8σ (5σ , 18.2 excess counts) and 4.6σ (4.3σ , 6.7 excess counts), respectively, confirming the hard photon spectrum.

Light curve Fitting

The characterization of P2 was performed via an unbinned likelihood fit of an asymmetric Lorentzian function [6, 15]. The fit to data selected above 5 TeV resulted in a position $\phi_{\text{P2}}^{\text{TeV}} = 0.568_{-0.003}^{+0.003}$, and a sharp outer edge (or trailing edge), $\sigma_{\text{T}}^{\text{TeV}} = 0.004_{-0.004}^{+0.006}$, both of which are compatible with the fitted values obtained above

²The number of trials is conservative for two reasons: (i) the 4 samples have overlapping energy ranges; and (ii) the 3 periodicity tests do not amount to 3 plain trials as they use exactly the same data sample.

Threshold Energy (TeV)	C-test σ	H-test σ	LR σ	Excess
0.5	3.7 (4.3)	2.7 (3.4)	3.8 (4.4)	23.2
1	4.3 (4.8)	2.1 (3.0)	3.8 (4.4)	19.7
3	4.9 (5.4)	3.9 (4.5)	4.7 (5.2)	18.2
5	5.8	4.7	5.0	14.3
7	5.6 (6.0)	4.5 (5.0)	4.8 (5.3)	14.0
20	4.6	3.1	4.3	6.7

Table M1 Significance levels obtained for different periodicity tests: the C-test, the H-test, and a maximum likelihood-ratio (LR) test. The parameters for the C-test ($\phi_{P2}^{\text{GeV}} = 0.565$, and $w = 0.025$ (FWHM)) and for the LR test (*On-* and *Off-*phase intervals defined as [0.55,0.6] and [0.7,1.0], respectively) were derived from the *Fermi*-LAT phasogram above 10 GeV [15]. The tests were applied on data selected above increasing energy thresholds, four of which, 0.5, 1, 3 and 7 TeV, were defined *a priori* to search for pulsations. Their initial significance level (shown in parenthesis) is corrected for the number of trials which has been conservatively estimated to be 12 (4 energy thresholds and 3 tests, see text). The number of events in excess of the background quoted in the last column was estimated with the LR test.

20 GeV, i.e., $\phi_{P2}^{\text{GeV}} = 0.565 \pm 0.001$ and $\sigma_T^{\text{GeV}} = 0.003 \pm 0.001$ [15]. The central fitted value of the inner edge width (or leading edge) of the TeV pulse, $\sigma_L^{\text{TeV}} = 0.007_{-0.004}^{+0.007}$, was found to be slightly smaller than $\sigma_L^{\text{GeV}} = 0.017 \pm 0.002$, but the difference is not statistically significant ($< 1.5\sigma$).

The fact that only P2 is detected in the multi-TeV range is consistent with the evolution of the phasogram with increasing energy. Indeed, the ratio of P1 / P2 amplitudes decreases with increasing energy, with P1 dominating below 300 MeV, while P3 dims and slides to later phases with increasing energy [6]. This trend was confirmed in the tens of GeV range [15], P2 being the sole significant feature in Vela’s phasogram there.

Spectral Derivation

Data were selected for the P2 and *Off-*phase intervals, defined as [0.55-0.6] and [0.7-1.0], respectively. The energy spectrum was derived using a maximum likelihood fit

within a forward-folding scheme, assuming *a priori* spectral models [86]. Instrument response functions (IRFs) were computed through extensive MC simulations as a function of the energy, zenith and azimuthal angles of the telescope pointing direction, the impact parameter of showers, and the configuration of the telescope array for each observing period.

The fit of a power law to the overall data set in the 660 GeV – 28.5 TeV energy range resulted in a very hard spectrum with photon index $\Gamma_{\text{VHE}} = 1.4 \pm 0.3^{\text{stat}} \pm 0.1^{\text{syst}}$ and normalization $\Phi_0 = (1.74 \pm 0.52^{\text{stat}} \pm 0.35^{\text{syst}}) \times 10^{-15} \text{ erg}^{-1} \text{ cm}^{-2} \text{ s}^{-1}$ at the decorrelation energy $E_0 = 4.24 \text{ TeV}$. This corresponds to an isotropic luminosity $L_{20\text{TeV}} \simeq 2 \times 10^{30} \text{ erg s}^{-1}$ for the source distance of 287 pc [14]. The systematic uncertainties on these results have been adopted from the study carried out in [75]. The limited statistics do not allow a test for a statistically significant deviation from the power-law hypothesis. We adopt conservatively 20 TeV as the maximum detected energy for individual photons in the following sections, noting that the energy spectrum extends up to 28.5 TeV due to events displaying an energy beyond 20 TeV.

Supplementary Material

The Multi-TeV Component

The TeV emission is most likely produced by inverse-Compton (IC) scattering of low-energy photons by energetic electrons. The target photons in Vela might consist of the observed non-thermal X-rays [24, 25], UV [26], and optical [27, 28] to near-infrared [29] emission (O-NIR), or thermal X-rays from the neutron star surface [25]. The spectral measurements from UV to NIR have shown a flat $F(\nu)$ spectrum ($\alpha_\nu = 0.01$) in the range $\epsilon \in [0.6, 10]$ eV ($\log_{10}(\nu/\text{Hz}) = 14.15 - 15.4$) [29]. These photons are generally considered as being emitted through SR of secondary pairs. In the magnetospheric scheme, secondary pairs are produced along the outer gaps (e.g. [21, 87]), or between the NS surface and $\sim 0.5 R_{LC}$, as assumed in [33]. In the wind-based framework, pairs are produced around the current sheet and their synchrotron emission develops as an isotropic radiation field in the optical to IR domains, as first proposed in [37] and investigated in recent PIC simulations [57, 69].

The scattering regime depends on the target photon energy in the center-of-momentum frame, $\gamma\epsilon$, and takes place in the Thomson or deep Klein-Nishina (K-N) regimes for $\gamma\epsilon \ll m_e c^2$ and $\gamma\epsilon \gg m_e c^2$, respectively. The lowest energy photons measured from Vela lie in the NIR domain at an energy of ~ 0.6 eV, together with two other measurements at 0.33 and 0.2 eV, though with lower precision [29]. This means that for the lower bound of the (measured) NIR radiation field the scattering takes place already in the mildly relativistic case. The luminosity in the O-NIR range, $L_{0.6\text{eV}} \simeq \omega_{\text{IR}} 2.3 \times 10^{28} \text{ erg s}^{-1}$, (where $\omega_{\text{IR}} < 1$ corrects for the solid angle) is two to

three orders of magnitude below that in the thermal, $L_X^{\text{th}} \simeq 8 \times 10^{31} \text{ erg s}^{-1}$, and non-thermal X-rays, $L_X \simeq \omega_X 10^{31} \text{ erg s}^{-1}$. However, for photons beyond the optical range, e.g. with energy $\epsilon > 10 \text{ eV}$, the IC emissivity is strongly suppressed due to the severe drop in the IC scattering cross section, $\sigma_{\text{KN}}/\sigma_{\text{T}} \lesssim 10^{-5} - 10^{-6}$. Hence the O-NIR photons are the dominating targets for efficient IC emissivity, noting that some contribution is also expected from the extreme K-N regime [87]. The VHE photon energy $E_{\text{VHE}} \simeq \gamma m_e c^2$ is thus set by γ .

The highest photon energies observed by H.E.S.S. imply a lower limit on the maximum particle energies of $\gamma_{\text{IC}}^{\text{max}} \gtrsim 4 \times 10^7 (E_{\text{VHE}}/20 \text{ TeV})$. When taking into account the spectral shapes of both GeV and TeV components, Lorentz factors of $\gtrsim 7 \times 10^7$ are needed to reproduce the data in the TeV range (see below).

The GeV Component

When considering pulsar gaps, electrons are believed to be accelerated by the component of the electric field parallel to the local magnetic field, E_{\parallel} , and radiating in the GeV regime mainly through CR. The maximum achievable Lorentz factor $\gamma_{\text{CR}}^{\text{max}}$ is limited by radiation reaction and not by escape from the acceleration region. Equating the energy loss and gain rates ($\frac{2}{3} \frac{e^2 c}{\rho_c^2} \gamma^4 = e c E_{\parallel}$), results in an expression of γ_c^{CR} as a function of the magnetic field B and curvature radius ρ_c , as $\gamma_{\text{CR}}^{\text{max}} = \left(\frac{3\eta B}{2e}\right)^{1/4} \rho_c^{1/2}$, where η is the magnetic conversion efficiency, $E_{\parallel} = \eta B$ ³. The magnitude of η depends on the particular version of the acceleration gaps with values usually assumed to be below 10% [33, 45] at the LC, although in some models values as large as 30% are used [41, 88]. The radius of curvature can be expressed in units of the LC radius

³For simplicity we use a constant value for E_{\parallel} along the field lines in the gap, as usually done in magnetospheric models.

($\rho_c = \xi R_{\text{LC}}$, with $R_{\text{LC}} = cP/2\pi$, and P the period of the pulsar). Assuming a static dipole geometry for the magnetic field, $B(r) = B_{\text{ns}}(R_{\text{ns}}/r)^3$, with B_{ns} and R_{ns} the surface magnetic field and the neutron star radius, respectively, $\gamma_{\text{CR}}^{\text{max}}$ can be expressed as $\gamma_{\text{CR}}^{\text{max}} = (3\pi/ce)^{1/4} \xi^{1/2} \eta^{1/4} B_{\text{ns}}^{1/4} R_{\text{ns}}^{3/4} P^{-1/4}$.

Using the inferred value of B_{ns} , the assumed value of R_{ns} and the measured period P for Vela (2.47×10^{12} G, 12 km and 89 ms, respectively), $\gamma_{\text{CR}}^{\text{max}}$ and the corresponding CR photon energy $E_{\text{CR}}^{\text{max}}$ for emission regions close to the LC can be written as:

$$\gamma_{\text{CR}}^{\text{max}} \simeq 4 \times 10^7 \xi^{1/2} \eta_{-1}^{1/4} \quad (\text{M1})$$

$$E_{\text{CR}}^{\text{max}} \simeq 5 \text{ GeV } \xi^{1/2} \eta_{-1}^{3/4} \quad (\text{M2})$$

with $\eta_{-1} = \eta/0.1$.

Assuming that CR is the dominating radiation process forming the HE spectral component, a mono-energetic beam of particles with $\gamma = \gamma_{\text{CR}}^{\text{max}} \sim 4 \times 10^7$ would contribute near $E_{\text{CR}}^{\text{peak}} \sim E_{\text{CR}}^{\text{max}}$. Given the measured $E_{\text{HE}}^{\text{peak}} \simeq 1.5 \text{ GeV}$ [5, 6, 15], for an emission taking place near the LC, $\xi \sim 1$, values of $\eta < 0.1$ and Lorentz factors $< 4 \times 10^7$ are implied (see Fig. M1). An estimate of the number of the contributing electrons can be obtained from the inferred luminosity $L_{1.5 \text{ GeV}} \simeq \omega_{\text{HE}} 9 \times 10^{33} \text{ erg s}^{-1}$ (where $\omega_{\text{HE}} < 1$ corrects for the solid angle) and given the curvature energy loss rate, $\left. \frac{-dE}{dt} \right|_{\text{CR}} = \frac{2}{3} \frac{e^2 c}{\xi^2 R_{\text{LC}}^2} \gamma^4 \simeq 6.5 \times 10^4 (\gamma/(4 \times 10^7))^4 \xi^{-2} \text{ erg s}^{-1}$ as: $N_0^{\text{CR}} \sim L_{1.5 \text{ GeV}} / \left(\left. \frac{-dE}{dt} \right|_{\text{CR}} \right) \simeq \omega_{\text{HE}} \xi^2 1.4 \times 10^{29}$ particles.

Alternatively, the GeV component can be interpreted as SR, if considering non-ideal MHD plasma conditions ($E > B_{\perp}$) deep in the reconnection layers to promote the maximum energy beyond the maximum reachable synchrotron energy ($\simeq 160$

MeV)[50]. In such a scenario, the peak of the GeV component would correspond to the characteristic energy $E_{\text{SR}}^{\text{max}} \sim E_{\text{HE}}^{\text{peak}} \simeq 1.5 \text{ GeV}$, with

$$\gamma_{\text{SR}}^{\text{max}} \simeq 1.3 \times 10^6 (B_{\perp}/B_{\text{LC}})^{-1/2} (E_{\text{SR}}^{\text{max}}/1.5 \text{ GeV})^{1/2} \quad (\text{M3})$$

where $B_{\text{LC}} = 5.53 \times 10^4 \text{ G}$ is the magnetic field intensity at the LC.

The SR energy loss rate, $\frac{-dE}{dt}|_{\text{SR}} \simeq 5 \times 10^6 (\gamma/1.3 \times 10^6)^2 \text{ erg s}^{-1}$ is two orders of magnitude larger than in the CR case, which implies in this case a smaller number of particles, $N_0^{\text{SR}} \sim L_{1.5\text{GeV}}/(\frac{-dE}{dt}|_{\text{SR}}) \simeq \omega_{\text{HE}} 1.8 \times 10^{27}$, involved in the GeV radiation.

The CR/IC and SR/IC scenarios

Given the phase alignment of the GeV and TeV pulsations, we assume that the same population of electrons, within an energy range partially or completely in overlap, and from similar spatial regions, is at the origin of the two components. The emission regions do not necessarily have to be identical as photons from radially extended zones can arrive at Earth at similar phases, i.e. form caustics, thanks to special-relativistic effects and the B -field structure, within (or slightly beyond) the magnetosphere [61–66], or within the equatorial CS in the near wind zone [53, 69].

Using the results obtained above, we can derive some constraints on the target radiation field energy density, and thereby, on the effective volume of the IC emission region V_{IC} in both SR/IC and CR/IC scenarios. We first consider IR to optical target photons and restrict the computations to the deep K-N regime, i.e. $\gamma \epsilon \sim 10 \times m_e c^2$, and hence the energy range to $(\epsilon_{\text{min}}, \epsilon_{\text{max}}) = (0.1, 4) \text{ eV}$. The energy loss rate in the extreme K-N limit is given by [89]: $\frac{-dE}{dt}|_{\text{IC}} \simeq \zeta (3/8) \sigma_{\text{T}} c m_e^2 c^4 \int_{\epsilon_{\text{min}}}^{\epsilon_{\text{max}}} \frac{n(\epsilon)}{\epsilon} [\log(\Gamma_e) - 11/6] d\epsilon$ where $\zeta < 1$ represents an overall efficiency factor for the IC scattering (i.e.

anisotropy, target photon direction/opening angle with respect to the accelerating field direction, etc), $\Gamma_e = \frac{4\epsilon\gamma}{m_e c^2}$, and $n(\epsilon)$ is the target photon density ⁴.

The target radiation field displays a photon index of $\alpha = \alpha_\nu + 1 = 1.01 \pm 0.01$ in the optical to IR range, and a luminosity of $L_{0.6\text{eV}} \simeq \omega_{\text{IR}} 2.3 \times 10^{28} \text{ erg s}^{-1}$ [29]. The target photon density $n(\epsilon)$ depends inversely on the effective interaction volume V_{IC} . This is also the case for the IC luminosity $L_{\text{IC}}^{\text{KN}} = N_0^{\text{IC}} \frac{-dE}{dt} \Big|_{\text{IC}} = L_{20\text{TeV}} \simeq \omega_{\text{VHE}} 2 \times 10^{30} \text{ erg s}^{-1}$. Assuming the same solid angle for the GeV and TeV emissions, $\omega_{\text{HE}} = \omega_{\text{VHE}}$, and using the number of emitting particles N_0^{CR} and N_0^{SR} derived above in the CR and SR scenarios, the required energy density of the target field could be expressed for each case as:

$$U_\epsilon^{\text{CR}} \simeq 3.8 \times 10^{13} \text{ eV cm}^{-3} \frac{1}{\zeta \xi^2} \left(\frac{L_{\text{IC}}^{\text{KN}}}{2 \times 10^{30} \text{ erg/s}} \right) \left(\frac{N_0^{\text{CR}}}{1.4 \times 10^{29}} \right)^{-1} \quad (\text{M4})$$

and

$$U_\epsilon^{\text{SR}} \simeq 3.0 \times 10^{15} \text{ eV cm}^{-3} \frac{1}{\zeta} \left(\frac{L_{\text{IC}}^{\text{KN}}}{2 \times 10^{30} \text{ erg/s}} \right) \left(\frac{N_0^{\text{SR}}}{1.8 \times 10^{27}} \right)^{-1} \quad (\text{M5})$$

Assuming a crossing time $t_c = \tau R_{\text{LC}}/c$, where $\tau < 1$ marks the uncertainty on emitting zone dimensions, and writing $U_\epsilon = L_{0.6\text{eV}} \times t_c / V_{\text{IC}}$, one obtains the following constraints:

$$V_{\text{IC}}^{\text{CR}} \sim v \tau \xi^2 \zeta \omega_{\text{IR}} 5.3 \times 10^{24} \text{ cm}^3 \quad (\text{M6})$$

$$V_{\text{IC}}^{\text{SR}} \sim v \tau \zeta \omega_{\text{IR}} 6.8 \times 10^{22} \text{ cm}^3 \quad (\text{M7})$$

where $v > 1$ is a correction factor to take into account the impact of the lower bound of the target photon energy range on the IC luminosity, e.g. a factor as high

⁴The spectral fits use a more detailed calculation including an extension to $\epsilon_{\text{min}} = 0.005 \text{ eV}$ and using the full K-N cross section formula.

as $v \sim 10$ for $\epsilon_{\min} = 0.005$ eV, as illustrated through spectral fits further below. Considering a particle density $n_{\text{tot}}^{\text{LC}} \sim \kappa_4 n_{\text{GJ}}^{\text{LC}} \simeq \kappa_4 4.3 \times 10^8 \text{ cm}^{-3}$ near the LC, where $n_{\text{GJ}}^{\text{LC}}$ is the Goldreich–Julian particle density and $\kappa_4 = \kappa/10^4$ the pair multiplicity, the effective volumes $V_{\text{IC}}^{\text{CR}}$ and $V_{\text{IC}}^{\text{SR}}$ contain the total number of particles $N_{\text{tot}}^{\text{CR}} \sim n_{\text{LC}}^{\text{tot}} V_{\text{IC}}^{\text{CR}} \sim 2.3 \times 10^{33}$ and $N_{\text{tot}}^{\text{SR}} \sim n_{\text{tot}} V_{\text{IC}}^{\text{SR}} \sim 2.9 \times 10^{31}$ for the CR/IC and the SR/IC scenarios, respectively. The particles contributing to the peak of the HE and VHE components represent then a fraction $N_0^{\text{CR}}/N_{\text{tot}}^{\text{CR}} \sim N_0^{\text{SR}}/N_{\text{tot}}^{\text{SR}} \sim 10^{-4}$ (up to the respective correction factors in Eqs. M6, M7) of the total number of particles available near the LC.

The effective volume under the CR/IC hypothesis $V_{\text{IC}}^{\text{CR}}$ is of the same order as the SR emitting volume mentioned in [33], i.e. $V^{\text{SR}} \sim \frac{\pi (0.5 R_{\text{LC}})^4}{2 R_{\text{LC}}} (r_{\text{out}}^2 - r_{\text{in}}^2) \simeq 3 \times 10^{23} \text{ cm}^3$, but the unknown magnitude of $v \tau \xi^2 \zeta \omega_{\text{IR}}$ makes any further comparison difficult. In the SR/IC framework, target photons are produced around the current sheet and the IC interaction can be assumed to be isotropic, hence $\zeta \omega_{\text{IR}} \sim 1$. As suggested by PIC simulations, the layer thickness δ can be estimated from the fiducial Larmor radius of the electrons accelerated in the open field line region beyond the LC [47, 69], $\rho_L = \gamma m_e c^2 / (e B_{\text{LC}}) \sim \delta \simeq 4 \times 10^4 \text{ cm}$ for $\gamma_c^{\text{SR}} \simeq 1.3 \times 10^6$. This corresponds to a SR emission volume $V^{\text{SR}} \sim \delta \times R_{\text{LC}}^2 \simeq 1.2 \times 10^{22} \text{ cm}^3$, which is of the same order as the constraint in Eq. (M7).

Heuristic spectral models

To further explore the implications of the H.E.S.S. data, we perform a joint fit to the HE and VHE components thus taking their spectral features into account. The limited statistics of the H.E.S.S. measurement only allows the fitting of a power-law function

to the data. Consistently, we assume for the energy distribution of the IC emitting particles the functional form:

$$\frac{d^2N}{d\gamma dt} \propto (\gamma/\gamma_0)^{-p} \exp [-(\gamma/\gamma^{\max})^\beta] \quad (\text{M8})$$

where the argument of the (super-) exponential cutoff represents $\gamma_{\text{CR}}^{\max}$ or $\gamma_{\text{SR}}^{\max}$, which are identified with $\gamma_{\text{IC}}^{\max}$ in the CR/IC and SR/IC schemes, respectively.

In the CR/IC scenario, the inverse-squared dependence of the CR energy loss rate on radius of curvature, $-\frac{dE}{dt}|_{\text{CR}} \propto \rho_c^{-2} \propto \xi^{-2}$ (see above), implies a narrow distribution for the trajectories of particles contributing most to the GeV component, and hence also for the energy distribution of particles (see, e.g., Fig. 11 in [45]). For the computation of CR, we consequently limit the extent of the particle distribution at its lower energy bound to $\gamma_{\text{CR}}^{\max}/10$, and define an effective radius of curvature $\hat{\rho}_c$ (or the scaled radius $\hat{\xi}$) representing the particle trajectories which contribute to the peak near $E_{\text{HE}}^{\text{peak}} \simeq 1.5 \text{ GeV}$, i.e. for which $E_{\text{CR}}^{\max} \sim 1.5 \text{ GeV}$. As discussed above, for a given E_{CR}^{\max} there is a degeneracy between values of η and ξ , which also determine the maximum Lorentz factor $\gamma_{\text{CR}}^{\max}$ (Eq. M1). We consider two cases. First, the emission is hypothesized to take place near the LC, i.e. $\hat{\xi} \sim 1$. The fit is constrained by the GeV data in this case and results in $\eta \simeq 0.02$ and $\gamma_{\text{CR}}^{\max} \simeq 2.8 \times 10^7$ (shown by a gray cross in Fig. M1). The latter value, when identified to $\gamma_{\text{IC}}^{\max}$, is insufficient to reproduce the VHE data (see curve labeled I_a in Fig. 3 of the main text). In the second case, the maximum Lorentz factor of IC-emitting particles is also constrained through the fit to the TeV component which results in $\gamma_{\text{IC}}^{\max} \gtrsim 7 \times 10^7$. Different combinations of $(\eta, \hat{\xi})$ can satisfy this condition, granted that $\eta \ll 0.1$ and $\hat{\xi} \gg 1$.

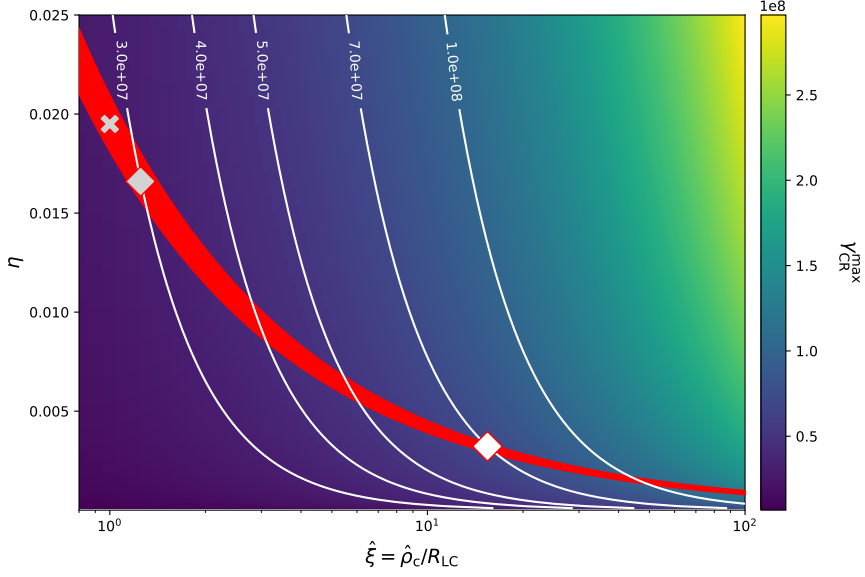


Fig. M1 Constraints in the CR/IC scenario on magnetic conversion efficiency. The maximum achievable Lorentz factor for electrons, $\gamma_{\text{CR}}^{\text{max}}$ is shown in color scale (increasing contours levels are shown as white curves) as a function of magnetic conversion efficiency η , and scaled curvature radius, $\hat{\xi}$. The red curve shows $(\eta, \hat{\xi})$ values when fitting the HE peak, i.e. they correspond to particle trajectories which contribute most to the HE peak, $E_{\text{CR}}^{\text{max}} \sim E_{\text{HE}}^{\text{peak}} \simeq 1.5$ GeV. The thickness of the red curve illustrates the uncertainty on HE peak energy ($\sim \pm 10\%$). The gray cross shows the solution $(\eta, \hat{\xi}) \sim (0.02, 1)$ yielding $\gamma_{\text{CR}}^{\text{max}} \simeq 2.8 \times 10^7$, while the gray and white diamonds correspond to curves I_a and I_c in Fig. 3 of the main text with $\gamma_{\text{CR}}^{\text{max}} \simeq 3 \times 10^7$ and 7×10^7 , respectively.

These combinations (which lie on the red curve in Fig. M1 to the right side of the white diamond) imply a dissipation region located beyond the LC⁵ where open field lines reach curvature radii well above R_{LC} and can provide for acceleration to higher energies than traditionally assumed in the magnetospheric picture⁶. The solution corresponding to $(\eta \simeq 0.003, \hat{\xi} \simeq 15)$ is marked as a white diamond in Fig. M1 and is shown in Fig. 3 of the main text in two versions: for the curve labeled I_b the IC component is calculated using O-NIR target photon field, while for I_c it is extended to the FIR. The

⁵Given the inclination and viewing angles in Vela ($\sim 70^\circ$ and $\sim 65^\circ$, respectively), the open field lines of interest cross the LC surface at radial distances not much larger than R_{LC} .

⁶We note, however, that more complicated schemes such as the non-stationary gap model as adopted in [43] and having recourse to a combination of different particle injection rates could still accommodate the data.

comparison of these two curves illustrates the impact of the target energy range on the TeV luminosity, i.e. a gain in luminosity of almost an order of magnitude for the extrapolated target energy range. The luminosity of the IC component depends also strongly on the effective interaction volume which is a complex quantity to tightly constrain. The normalization of the models is hence (almost) a free parameter in the spectral fits. On the other hand, the parameters of the energy distribution of the parent population can be constrained by the joint fit, though not unambiguously given both the correlation between the spectral index p and the exponential power β , and the limited extent of the distribution itself towards lower energies (see above). For the two solutions ($\eta \simeq 0.02, \hat{\xi} \simeq 1$) and ($\eta \simeq 0.003, \hat{\xi} \simeq 15$) we obtain $(p, \beta) \simeq (0.6, 1.9)$ and $\simeq (1.1, 2.0)$, respectively. For both solutions, we note a power deficit in the lower energy part of the HE spectrum (< 1 GeV) as compared to the data. This deficit is usually attributed to the SR contribution to this part of the spectrum (globally modeled as synchro-curvature radiation, SCR see e.g. [90]), which is not included in the spectral model. Predicted spectral energy distributions (SEDs) taken from two recently published models adopting more sophisticated CR/IC and SCR/IC schemes and including computation of light curves [33, 87] are shown in Fig. M2⁷.

In the SR/IC scenario, the formation of a hard power-law particle spectrum, i.e. with index $p \in [1, 2]$, is expected from PIC simulations of acceleration via relativistic magnetic reconnection (e.g., [52–54, 57]). Accordingly, we use a larger energy span (few 10^5) for particles as compared to the CR case. As for the IC target photon field energy span, we limit the computations to the measured O-NIR domain. Using an

⁷Inspired by the first preliminary announcement of a H.E.S.S. multi-TeV signal [91].

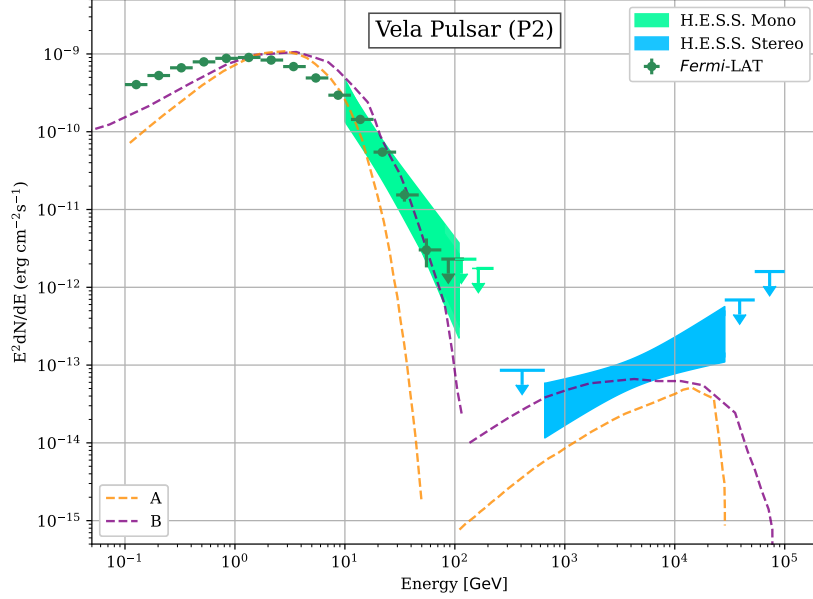


Fig. M2 SEDs from two publications in the CR/IC and SCR/IC schemes compared to the Vela data. *Data:* see Fig. 3. *Curves:* Two recently published models are compared to the Vela SED. Curve A shows the phase-resolved SED of an outer-gap-based CR/IC model applied to Vela P2 [87]. The curve labeled B corresponds to the re-scaled version of a phase-averaged computation based on a separatrix/CS scenario [33] where primary particles are predominantly accelerated in the CS, though not through magnetic reconnection. Here, particles are cooled via SCR in the MeV and GeV ranges. Both models predict a GeV peak energy ($E_{\text{HE}}^{\text{peak}} \gtrsim 3 \text{ GeV}$) larger than that measured by *Fermi*-LAT, i.e. they do not lie on the red curve in Fig. M1, hence providing for larger maximum Lorentz factors γ^{max} for IC-emitting particles. The target SR photon spectrum is extrapolated for both models to the FIR ($\epsilon_{\text{min}} = 0.001$ and 0.005 eV , for curves A and B, respectively).

exponentially cutoff power law for the particle energy distribution (see the functional form M8 given above), the fit of the resulting SR component to the GeV data yields shape parameters $p \simeq 1$, $\beta \simeq 1.8$ and $\gamma_{\text{SR}}^{\text{max}} \simeq 1.3 \times 10^6$ (see Eq. M3). In this case,

the spectral model fits the HE data in the < 1 GeV range without requiring an additional SCR component. The best-fit cutoff value with the (super-) exponential form is, however, well below the value $\gamma_{\text{IC}}^{\text{max}} \gtrsim 7 \times 10^7$ required by the H.E.S.S. measurement (see curve labeled II_a in Fig. 3 of the main text). For the SR/IC scenario to reproduce the H.E.S.S. data, IC emitting particles must therefore have a significantly higher energy cutoff than the one deduced from the SR cooling. PIC simulations have confirmed that the acceleration and SR cooling processes take place in subsequent steps and different regions [92]. Recent studies including synchrotron cooling and pair production have further shown that the highest energy particles are not trapped by the magnetic loops (or plasmoids/magnetic islands) but accumulate in their vicinity where the magnetic field intensity is weak and the SR cooling is inefficient [57]. Hence they can reach energies well beyond the SR burn-off limit $\gamma_{\text{SR}}^{\text{max}}$ and exceeding the magnetization $\sigma_{\text{LC}} \simeq 7 \times 10^5$ at LC⁸. For this to happen, the Larmor radius of such particles, $\rho_L \simeq 4 \times 10^{-3} R_{\text{LC}} (\gamma^{\text{max}}/7 \times 10^7)$, should be larger than the size of the largest plasmoids. Alternatively, cooled particles could be re-accelerated further in the CS layers and produce an IC emission in a second step. In any case the phase coherence of the SR and IC pulses should be preserved, given the phase alignment of the HE and VHE components in the data. The formation of caustics for emission loci in the $1 - 2 R_{\text{IC}}$ region as shown in PIC studies makes such scenarios plausible [53]. The IC cooling time for particles with $\gamma^{\text{max}} \sim 10^8$ scattering $\epsilon = 0.1$ eV targets, $t_{\text{IC}} \sim 50$ ms, is of the order of the pulsar period, and hence compatible with the above schemes. For generating the spectral model corresponding to this picture, we assume

⁸The magnetization at the LC is defined through Michel's magnetization parameter μ_{M} as: $\sigma_{\text{LC}} \sim \mu_{\text{M}} = B_{\text{LC}}^2 / (4 \pi \kappa_4 n_{\text{GJ}}^{\text{LC}} m_e c^2) \simeq 7 \times 10^5$ (e.g., [47, 57, 93]).

that the particles with energies beyond $\gamma_{\text{SR}}^{\text{max}}$ are from the same population as the one emitting SR, of which the energy spectrum is extended to beyond the SR cooling energy. The fit to the TeV data (shown for $\gamma^{\text{max}} \sim 10^8$ and labeled II_b in Fig. 3 of the main text) results in an interaction volume $V_{\text{IC}}^{\text{SR}} \simeq 1.5 \times 10^{23} \text{ cm}^3$. This corresponds, as expected, to a larger volume than that estimated above, as the highest energy particles must have larger Larmor radii than those trapped and cooled through SR in the plasmoids. Various uncertainties, e.g. the correction factor $v\tau$ ($\zeta\omega_{\text{IR}} \sim 1$, see above) or the unknown lower bound of the target field energy range, make it difficult to go beyond this order-of-magnitude comparison.

The bulk movement of the striped wind, with Lorentz factor Γ_{w} , can affect the physical picture due to the Doppler boosting of radiations [23, 46, 48, 49, 58–60]. In such a scheme, SR and IC take place in the wind co-moving frame where electrons are assumed to have an isotropic distribution. The observed emission is obtained after Doppler boosting of the quantities into the laboratory frame. Assuming $B(\hat{r}) \sim B_{\text{LC}}/\hat{r}^2$ in the near wind region (e.g., [46]), and given the emission radius $\hat{r} = r/R_{\text{LC}}$, $B'(\hat{r}) = B(\hat{r})/\Gamma_{\text{w}}$, and $E_{\text{SR}}^{\text{max}'} = E_{\text{SR}}^{\text{max}}/2\Gamma_{\text{w}}$, one can rewrite (Eq. M3) as: $\gamma_{\text{SR}}^{\text{max}'} \simeq 10^6 \left(\frac{E_{\text{SR}}^{\text{max}}}{1.5 \text{ GeV}}\right)^{1/2} \hat{r}$. By requiring that the 20 TeV photons are produced by SR-emitting electrons, $\gamma_{\text{IC}}^{\text{max}} = 2 \times \Gamma_{\text{w}} \gamma_{\text{SR}}^{\text{max}'}$, one obtains a relation :

$$\Gamma_{\text{w}} \simeq 22 \left(\frac{E_{\text{SR}}^{\text{max}}}{1.5 \text{ GeV}}\right)^{-1/2} \left(\frac{E_{\text{VHE}}}{20 \text{ TeV}}\right) \hat{r}^{-1}. \quad (\text{M9})$$

The linear rise of the bulk Lorentz factor up to the fast magnetosonic point (e.g. [53]), $\Gamma_{\text{w}} = (1 + \hat{r}^2)^{1/2}$, provides a second constraint, leading to a solution: $\Gamma_{\text{w}} \simeq \hat{r}_e \simeq 5$. Taking into account the exact shape of the GeV component modifies this solution

somewhat, but the emission radius remains at a few R_{LC} . As an example, a fit to the data with $\Gamma_w = 10$ at $\hat{r}_e = 5$ is shown in Fig. 3 in the main text (curve labeled Π_c). A dissipation region at this distance is, however, not favored by PIC simulations which point to a SR emission region closer to the light cylinder (1 to 2 R_{LC}). An alternative boosted scenario, involving e.g. a re-acceleration of cooled particles, where SR and IC photons are emitted in separate zones could still be compatible with the above constraint if the formation of caustics provides the phase alignment of the two components.